

 Open access • Journal Article • DOI:10.1063/1.5054263

Temporal variation of the spatial density distribution above a nanosecond pulsed dielectric barrier discharge plasma actuator in quiescent air — [Source link](#)

Takahiro Ukai, Andrew Russell, Hossein Zare-Behtash, Konstantinos Kontis

Institutions: Osaka Institute of Technology, University of Glasgow

Published on: 21 Nov 2018 - Physics of Fluids (AIP Publishing LLCAIP Publishing)

Topics: Plasma actuator, Dielectric barrier discharge, Plume, Ion wind and Plasma

Related papers:

- [Numerical investigation of nanosecond pulsed plasma actuators for control of shock-wave/boundary-layer separation](#)
- [Jet flow induced by a surface plasma actuator](#)
- [Measurements of the Propagation Velocity of an Atmospheric-Pressure Plasma Plume by Various Methods](#)
- [Development and characterization of a multi-electrode cold atmospheric pressure DBD plasma jet aiming plasma application](#)
- [Charge dependence of the plasma travel length in atmospheric-pressure plasma](#)

Share this paper:    

View more about this paper here: <https://typeset.io/papers/temporal-variation-of-the-spatial-density-distribution-above-4r63nitsfj>



Ukai, T., Russell, A., Zare-Behtash, H. and Kontis, K. (2018) Temporal variation of the spatial density distribution above a nanosecond pulsed dielectric barrier discharge plasma actuator in quiescent air. *Physics of Fluids*, 30(11), 116106. (doi:[10.1063/1.5054263](https://doi.org/10.1063/1.5054263))

This is the author's final accepted version.

There may be differences between this version and the published version. You are advised to consult the publisher's version if you wish to cite from it.

<http://eprints.gla.ac.uk/173912/>

Deposited on: 22 November 2018

Enlighten – Research publications by members of the University of Glasgow
<http://eprints.gla.ac.uk>

1 **Temporal variation of the spatial density distribution above a**
2 **nanosecond pulsed dielectric barrier discharge plasma actuator in**
3 **quiescent air**

4
5 Takahiro Ukai^{1*}, Andrew Russell², Hossein Zare-Behtash², Konstantinos Kontis²

6 1 *Osaka Institute of Technology, Osaka, 535-8585, Japan*

7 2 *University of Glasgow, School of Engineering, Glasgow, G12 8QQ, UK*

8
9 ***Corresponding author: *Takahiro Ukai***

10 **email:** *takahiro.ukai@oit.ac.jp*

11 **Telephone:** +81-(0)6-6954-4256

12 **Abstract:**

13 The thermal perturbation caused by a nanosecond pulsed dielectric barrier discharge (ns-DBD) plasma
14 actuator may lead to boundary layer transition. Hence, understanding of the thermal flow induced by
15 the ns-DBD plasma actuator will contribute to the development of an efficient flow control device for
16 various engineering applications. In this study, the spatial density distribution related to the thermal
17 flow was experimentally investigated using both qualitative and quantitative schlieren techniques. The
18 focus of this study is to understand the initial temporal variation of the spatial density distribution
19 above the ns-DBD plasma actuator in quiescent air. The quantitative visualisation showed that a hot
20 plume is generated from the edge of the exposed electrode and moves slightly towards the ground
21 electrode. A possible explanation is that an ionic wind and/or an induced jet leads to the movement of
22 the hot plume. However, the plasma-induced flow (the ionic wind and the induced jet) is generated
23 after the primary plasma discharges; namely, the hot plume does not move immediately after the first
24 plasma discharge. At almost the same time as the movement of the hot plume, consecutive plasma
25 discharges enhance the density of the hot plume; thereafter, the density reaches almost a steady state.

26 **Keywords:** **Flow control; ns-DBD plasma actuator; thermal convection; quantitative schlieren**

27 1. INTRODUCTION

28 Dielectric barrier discharge (DBD) plasma actuators are promising devices for flow control that can
29 be applied to a number of scenarios: flow separation postponement, turbulence augmentation, drag
30 reduction, and lift enhancement. Many numerical and experimental investigations have shown the
31 effectiveness of DBD plasma actuators for engineering applications; such as film cooling [1, 2], aircraft
32 wing [3-5], and ground vehicles [6, 7]. The experiment of Benard *et al.* [8] demonstrated that the DBD
33 plasma actuator placed on a NACA0015 aircraft wing delays the onset of stall by one or two degrees
34 and achieved approximately 30% drag reduction at a 15 degree incidence. According to Choi *et al.* [9],
35 multiple DBD plasma actuators would contribute to skin-friction reduction due to the induced quasi-
36 streamwise vortices in turbulent boundary layer. Moreover, Roy *et al.* [6] showed that a serpentine
37 DBD plasma actuator, positioned at the rear body of a lorry, induces the streamwise vortices and
38 demonstrated that a 10% drag reduction is achieved at a freestream velocity of 31.3 m/s. However,
39 what is important to note is that the aerodynamic performance depends on the actuator configuration
40 and the installation position [10-12], as well as electrical parameters: magnitude of input voltage,
41 frequency, and duty cycle *etc.* [8, 11-14]. Input voltage waveform has been shown to have a particularly
42 dramatic effect on induced-flow characteristics.

43 Nanosecond pulsed DBD (ns-DBD) plasma actuators are potentially applicable to the high-speed
44 flow regime. The previous studies demonstrated a nanosecond plasma actuator influences the flow
45 field at a Mach 0.85 [3] and a Mach 2.8 [15]. The ac-driven DBD (ac-DBD) plasma actuator, which is
46 excited by a sinusoidal input voltage signal, produces an ionic wind that induces a body force close to
47 the surface of the dielectric. However, the induced-flow velocity of the ac-DBD plasma actuator is in
48 the range of only a few meters per second (usually less than 10 m/s) in quiescent air [11], therefore its
49 application to high-speed flows is limited. On the other hand, the ns-DBD plasma actuator, which is
50 excited by short pulsed high voltage, in the order of nanoseconds, is applicable to the aerofoil flow
51 reattachment up to Mach 0.85 [3]. Instead of the body force, the ns-DBD plasma actuator provides
52 energy transfer which is a dominant induced-flow characteristic [16]. The rapid temperature increase,
53 caused by the high voltage energy deposition from the nanosecond pulsed discharge, which results in
54 shock wave formation due to the instantaneous heating of the gas. A hemi-cylindrical shock wave is
55 generated along the edge of the exposed electrode. Moreover, a plasma layer which propagates towards
56 the dielectric surface generates weak shock waves coalesce into a quasi-planar shock wave [17].
57 Therefore, the ns-DBD plasma actuator acts as a thermal energy source resulting in the rapid localised
58 heating of the near-surface gas layer at the plasma actuator. This outlines the difference in induced-
59 flow characteristics between the ac-DBD and ns-DBD plasma actuators.

60 The energy transfer generated by ns-DBD plasma actuators results in dominant flow control
61 authority. Induced flow characteristics in a quiescent gas condition were numerically and
62 experimentally investigated in the previous studies [18-20]. Zhao *et al.* [20] investigated a shock Mach
63 number in various input voltages and showed that the shock Mach number which depends on the input
64 voltages decays quickly and it propagates at approximately Mach 1 from 2 or 3 mm from the plasma
65 surface. Additionally, ns-DBD plasma actuators lead to thermal perturbation with the weak shock wave.
66 According to an experimental investigation in a quiescent gas condition [18], the area of the hot spot
67 expands with increase of the number of input voltage pulses within the burst. From the point of view
68 of flow modification, the weak shock wave should not strongly influence surrounding air at the high-
69 speed flow. However, the ns-DBD plasma actuator is applicable at a Mach 0.85 [3]. The reason why
70 the ns-DBD plasma actuators can change the surrounding flow is that the thermal perturbation plays a
71 key role rather than the shock wave.

72 To understand thermal flow induced under the uniform flow condition, the previous studies
73 attempted to investigate the effects of the thermal perturbation on surrounding air [18, 21-24]. Komuro
74 *et al.* [21] investigated the effect of the thermal perturbation on flow instability due to a ns-DBD plasma
75 actuator around aerofoil at 20 m/s and showed that the interaction of two different heated structures
76 improved the lift performance of the aerofoil. Correale *et al.* [18] investigated the influence of the
77 heated gas on a laminar boundary layer on a flat plate. They showed that the thermal perturbation
78 generated by the plasma discharge leads to a velocity fluctuation, and it is believed that the velocity
79 fluctuation results in a T-S (Tollmien-Schlichting) wave which causes laminar-turbulent transition of
80 the boundary layer. Therefore, the thermal perturbation plays a key role in the flow control mechanism
81 of the ns-DBD. The thermal perturbation is associated with the actuation frequency of the ns-DBD
82 plasma actuator, and the actuation frequency influences the boundary layer instability. According to an
83 experimental investigation regarding boundary layer transition by the ns-DBD plasma actuator [23],
84 the boundary layer transition point moves upstream when the actuation frequency increases. Moreover,
85 the thermal perturbation would create coherent vortices that increase the momentum transfer from the
86 freestream flow to the boundary layer. Such vortices generated by ns-DBDs also result in the
87 reattachment of the separated flow on an aircraft wing [24]. Additionally, a hot wire experiment by
88 Ullmer *et al.* [23] revealed that a ns-DBD plasma actuator excited velocity oscillations inside a
89 boundary layer. This means that the ns-DBD plasma actuators generate turbulent kinetic energy in the
90 boundary layer. Although the hot wire and liquid crystal techniques provide the valuable quantitative
91 information, the quantitative spatial measurement techniques lead to further understanding of
92 mechanism of the boundary layer transition.

93 The performance of the ns-DBD plasma actuator is significant in the high-speed flow regime and

94 the instant heating influences boundary layer transition. However, the mechanism by which the instant
95 heating affects the flow instability is not fully understood. The investigations about the thermal
96 distribution generated by the ns-DBD plasma actuator in the quiescent gas condition are important to
97 elucidate how the surrounding gas is heated and there is a local heat spot. It is believed that the
98 investigations of the thermal distribution in a quiescent gas condition lead to deeper understanding of
99 the mechanism of the boundary layer transition. Additionally, the previous investigations found that
100 thermal flow important for flow control rather than shock wave; however, the quantitative investigation
101 of the temporal and spatial variations of a density/temperature is necessary to further understanding
102 the mechanism of thermal flow by ns-DBD plasma actuator. In this study, to understand the thermal
103 perturbation induced by the ns-DBD plasma actuator, the spatial density field in quiescent air was
104 experimentally investigated using the qualitative and quantitative schlieren techniques.

105 **2. Experimental setup and diagnostics**

106 **2.1. Experimental model**

107 An ns-DBD plasma actuator shown in Fig.1 was used in the present study. In a previous study [25],
108 the effect of geometry on shock wave strength was investigated, and the results showed that the thicker
109 dielectric provides a stronger shock wave for a given input voltage and pulse frequency. The optimal
110 geometric parameters employed in the previous study (electrode thickness and electrode width) were
111 selected for the present investigation. The exposed high-voltage electrode of 5 mm in width and the
112 ground electrode of 10 mm in width were made of copper with thickness of 35 μm . The electrodes are
113 separated by a dielectric material (FR-4: Flame Retardant Type 4) with thickness of 0.4 mm. The
114 material of plasma actuator is manufactured by a company MG Chemicals. There is no discharge gap
115 between the electrodes. The lateral length of all electrodes is 90 mm. The ground electrode was fully
116 covered by three layers of polyimide film and the thickness of each polyimide film is approximately
117 70 μm . The polyimide film covered the exposed electrode 9 mm from both lateral side edges to avoid
118 a plasma discharge from the side edges, plasma releases from the exposed electrode of 72 mm in width.
119 The actuators were made using the process of double-sided photolithography. The masks for the
120 process were created using CAD software (SolidWorks) to ensure their accuracy as much as possible.
121 The copper comes with a photo resist coating, this is exposed under a UV light for 30 seconds. It is
122 then put in a developer bath that removes the resist that was exposed to the UV light. The developer
123 is Seno 4006, a solution of Potassium hydroxide, and Disodium metasilicate. The board is then sprayed
124 with a ferric chloride solution to remove the exposed copper. It takes approximately 1 minute per side
125 to remove the copper. Once the copper is removed, the remaining photo resist is cleaned with acetone.

126 The discharge is driven by a high-voltage nanosecond pulse generator (Megaimpulse, model: NPG-
127 18/3500(N)) that supplies negative pulse polarity at a pulse rise time of approximately 4 ns. In the
128 present study, an input voltage of 12 kV (negative polarity) was used with a pulse frequency of 1 kHz
129 controlled by a function generator (AIM & THURLBY THANDAR INSTRUMENTS, model:
130 TG2000). As the negative polarity produces large gross energy related to strong gas heating [26], thus
131 negative polarity was used in this study. The supplied high-voltage pulses were transferred from the
132 pulse generator to the exposed electrode by a 75 Ω coaxial cable.

133 The ambient temperature was monitored using a K-type thermocouple with a data acquisition
134 module system (National Instruments Corp., model: NI-9213, 24 bit) driven by LabVIEW. The
135 ambient pressure was measured by a Fortin mercury barometer. In the present experiment, the ambient
136 temperature and ambient pressure were 288.7 ± 0.3 K and 101.38 ± 0.03 kPa, respectively.

137 **2.2. Conventional schlieren photography**

138 The schlieren technique with a standard Z-type optical arrangement was employed to visualise the
139 qualitative density gradient above the ns-DBD plasma actuator that leads to the generation of a shock
140 wave as well as a thermal distribution. The schlieren system consists of a continuous light source
141 (Newport, model: 66921) with a 450 W Xe arc lamp, a condenser lens with a focal length of 70 mm,
142 a pinhole, a pair of 203.3 mm diameter concave mirrors with a focal length of 1829 mm, a circular dot
143 cut-off plate, an imaging lens, and a high-speed camera. The pinhole in front of the condenser lens
144 creates a light spot that illuminates the first concave mirror. The light beam is then collimated by the
145 first mirror and passes through the test section where the ns-DBD plasma actuator is located. The
146 collimated beam is reflected by the second concave mirror. The circular dot plate is positioned at the
147 focal point of the second mirror. The circular dot plate plays the same role as a knife edge, but the
148 density change in both directions on the x-y plane is made visible simultaneously. The imaging lens in
149 front of the camera focuses the image onto the camera sensor. The images were acquired using a 10
150 bit CMOS camera (Photron, model: FASTCAM-APX RS, maximum spatial resolution: 1024×1024
151 pixels) at a frame rate of 70 kfps with an exposure time of 1 μ s. An offset angle between the collimated
152 light beam and the light path from the light source to the first/second mirrors was set at 19 degrees to
153 prevent coma aberration. To transfer from pixels to millimetres, we took the image of an object where
154 the actual size was known. In colour schlieren mode, a three colour filter wheel was used as a substitute
155 for the circular dot plate. The colour images were recorded using a high resolution CMOS colour
156 camera (Canon, model: EOS 600D, 18 Mpixels resolution). The camera is set to continuous shooting
157 mode at 3.7 fps, while the shutter speed is set at a minimum of 0.25 ms. As the nanosecond pulsed
158 generators generate electromagnetic interference (EMI), the data acquisition system and camera were

159 covered using a metal mesh to minimize the effect of the EMI as much as possible.

160 **2.3. Calibrated schlieren photography**

161 The calibrated schlieren technique enables the measurement of the quantitative spatial density field
 162 above the ns-DBD plasma actuator. The optical arrangement of calibrated schlieren photography is
 163 shown in Fig. 2 which is the same as that of the conventional high-speed schlieren photography
 164 previously discussed. However, several optical items are difference between these setups. A graded
 165 filter, which plays the same role as a knife edge, was substituted for the circular dot plate, and the
 166 pinhole was replaced with a slit. The graded filter spreads the cut-off linearly in the beam focal plane
 167 and lessens the diffraction effect of the knife edge [27]. The graded filter and the slit were vertically
 168 positioned to measure a pixel intensity change in the x-direction, whereas they were horizontally
 169 positioned for a pixel intensity change in the y-direction. Both pixel intensity changes in the x- and y-
 170 components are necessary because the density gradient in the x- and y-components are apparent above
 171 the plasma actuator. The images were acquired using the same Photron camera (FASTCAM-APX RS)
 172 at a frame rate of 3 kfps with an exposure time of 22.11 μ s. This experiment focuses on the quantitative
 173 visualisation of the thermal distribution rather than shock wave propagation; therefore the exposure
 174 time is relatively longer than that used for shock wave visualisation.

175 The principle of the quantitative schlieren technique is explained here. The angle of the refraction
 176 ε obtained from refractive-index gradient integrated along the optical axis (the z-direction shown in
 177 Fig. 1) above the plasma actuator is expressed as;

$$\varepsilon_y = \frac{1}{n} \int_0^Z \frac{\partial n(x, y)}{\partial y} dZ = \frac{Z}{n_\infty} \frac{\partial n(x, y)}{\partial y} \quad (1)$$

$$\varepsilon_x = \frac{1}{n} \int_0^Z \frac{\partial n(x, y)}{\partial x} dZ = \frac{Z}{n_\infty} \frac{\partial n(x, y)}{\partial x} \quad (2)$$

178 The subscript ∞ denotes the quiescent surrounding gas, n is the local refractive-index. Since the knife
 179 edge alters the luminance depending on the refraction angle, schlieren photography presents an image
 180 where the pixel intensity is related to the refraction angle [27]. A calibration lens provides a
 181 quantifiable relationship between the refraction angle and the image pixel intensity [28]. The refraction
 182 angle ε provided by the calibration lens can be expressed as:

$$\varepsilon \approx \tan \varepsilon = r/f \quad (3)$$

183 where f and r are the focal length of the calibration lens and an arbitrary radius on the lens surface,
 184 respectively. A previous paper suggests using a calibration lens with a long focal length [28]. Having
 185 a longer focal length allows the uncertainty due to aberration to be neglected. This is because the focal

186 plane of the calibration lens is far away from the camera sensor. In the present experiment, a plano-
 187 convex lens (CVI Laser Optics, model: PLCX-25.4-5151.0-C, focal length: 10 m, outer radius: 12.7
 188 mm, surface accuracy: $\lambda/10$) was employed as the calibration lens. Figure 3 (a) shows the image pixel
 189 intensity provided by the calibration lens. The refraction angle ε_{image} appearing on the lens surface is
 190 expressed as equation (4).

$$\varepsilon_{image} = \varepsilon - \varepsilon_0 = \frac{1}{f}(r - r_0) \quad (4)$$

191 The subscript 0 denotes the defined centre of the calibration lens. Figure 3 (b) shows the measured
 192 value and a fitting curve by a cubic polynomial. The calibration curve (fitting curve) shown in Fig. 3
 193 (b) enables the conversion of image pixel intensity to refraction angle. In the present setup, the
 194 available calibration value of the refraction angle is in the range of 0.97416×10^{-3} and -1.2312×10^{-3}
 195 rad for the refractive index in the x-direction. Once the calibration value is obtained, the calibration
 196 lens is removed from the test section.

197 In the calibration process, the uncertainty of the refraction angle is mainly due to two factors: the
 198 approximation error of the fitting curve, and the detection error of a virtual centre of the calibration
 199 lens. The virtual centre of the calibration lens is the location where the pixel intensity appearing on the
 200 surface of the calibration lens matches the background pixel intensity around the lens. The background
 201 pixel intensity is not perfectly uniform due to the scattering of the light source, thus there is the
 202 possibility that the location of the virtual centre of the calibration lens moves. In equation (4), the
 203 virtual centre of the calibration lens related to r_0 has an error assumed as σ_{r_0} , which results in the error
 204 of the refraction angle. On the other hand, the fitting curve produces the uncertainty of the refraction
 205 angle. Although the fitting curve shown in Fig. 3 (b) shows good agreement with the experimental
 206 value, the approximation error cannot be neglected. The approximation error of the fitting curve
 207 calculated by RMSE (Root Mean Squared Error) as:

$$\sigma_{cal,y} = \sqrt{\frac{1}{N} \sum_{i=1}^N (\varepsilon_{exp,y}(\Delta I)_i - \varepsilon_{fit,y}(\Delta I)_i)^2} \quad (5)$$

$$\sigma_{cal,x} = \sqrt{\frac{1}{N} \sum_{i=1}^N (\varepsilon_{exp,x}(\Delta I)_i - \varepsilon_{fit,x}(\Delta I)_i)^2} \quad (6)$$

208 where N is the sampling number of the total obtained experimental values, ε_{exp} and ε_{fit} are the
 209 experimental and fitted calibration values, respectively. The subscript x and y denote the cut-off
 210 direction. Therefore, the uncertainty of the refraction angle due to the calibration process is estimated
 211 using equation (7) and (8).

$$\sigma_{\varepsilon,y} = \sqrt{(\sigma_{cal,y})^2 + \left[\left(\frac{\partial \varepsilon_{image,y}}{\partial r_{0,y}} \right) \cdot \sigma_{r0} \right]^2} \quad (7)$$

$$\sigma_{\varepsilon,x} = \sqrt{(\sigma_{cal,x})^2 + \left[\left(\frac{\partial \varepsilon_{image,x}}{\partial r_{0,x}} \right) \cdot \sigma_{r0} \right]^2} \quad (8)$$

212 Figure 4 shows the flow chart for the processing of the schlieren images. The schlieren images are
 213 captured using the vertical- and horizontal-cutoff orientations separately. To reveal the anticipated
 214 weak density change created by the actuator, an image distorted by the density change due to plasma
 215 actuation is subtracted from a reference image which is captured before the experiment; namely, the
 216 subtracted image pixel intensity is expressed as: $\Delta I(x, y) = I(x, y) - I_r(x, y)$, where I and I_r denote the
 217 distorted image intensity and the reference case, respectively. Based on the calibration curve, the
 218 subtracted image intensity $\Delta I(x, y)$ is converted to the refraction angle $\varepsilon(x, y)$. Each experiment was
 219 repeated three times to obtain an ensemble average of the local refraction angle $\hat{\varepsilon}(x, y)$. This process
 220 ensures the experimental repeatability. The derivative of the refractive index gradients forms an elliptic
 221 partial differential equation commonly known as the Poisson equation.

$$\frac{\partial^2 n(x, y)}{\partial x^2} + \frac{\partial^2 n(x, y)}{\partial y^2} = S(x, y) = \frac{n_\infty}{z} \left\{ \frac{\partial \hat{\varepsilon}_x(x, y)}{\partial x} + \frac{\partial \hat{\varepsilon}_y(x, y)}{\partial y} \right\} \quad (9)$$

222 where $S(x, y)$, which is the source term, is given by the refraction angle gradients obtained from the
 223 schlieren images. The Poisson equation is solved using the Successive Over-Relaxation method. The
 224 local refractive-index, which is computed based on the solution of the Poisson equation (9), is related
 225 to the gas density by the Gladstone-Dale law:

$$n = k \cdot \rho + 1 \quad (10)$$

226 The Gladstone-Dale constant for air, $k = 2.26 \times 10^{-4} \text{ m}^3/\text{kg}$, is applied in the calculation. Consequently,
 227 the spatial density distribution above the ns-DBD plasma actuator can be obtained.

228 2.4. Validation of the calibrated schlieren technique

229 Using the calibrated schlieren technique, the temperature distribution due to natural convection
 230 formed on an aluminum vertical hot plate of 150 mm \times 1.6 mm (width \times thickness) was measured and
 231 compared to a theoretical value to validate the present optical arrangement of calibrated schlieren
 232 photography. Based on a similarity solution of equation (11), the temperature T_{BL} in the thermal
 233 boundary layer formed on the vertical hot plate is calculated.

$$T_{BL} = H(\eta) \cdot (T_s - T_\infty) + T_\infty \quad (11)$$

234 The function H is obtained from reference [29], a Prandtl number $Pr = 0.72$ is used for the present

235 experiment. The similarity parameter η is expressed by Grashof number Gr at the distance y from the
 236 leading edge of the vertical hot plate,

$$\eta = \left(\frac{Gr}{4}\right)^{1/4} \cdot \frac{y}{x} \quad (12)$$

$$Gr = \frac{g \cdot \beta \cdot (T_s - T_\infty) \cdot x^3}{\nu^2} \quad (13)$$

237 where x , β , and ν are the perpendicular distance, thermal expansion, and kinematic viscosity,
 238 respectively. Gravity is taken as $g = 9.81 \text{ m/s}^2$. The vertical plate was heated by a silicone rubber heater
 239 glued on the backside of the vertical plate, and the surface temperature was adjusted to $T_s = 326 \text{ K}$
 240 using a DC power supply (Voltcraft, model: VSP 2410). The surface temperature was stable after the
 241 silicone rubber heater was switched on for more than 15 minutes. The surface temperature was
 242 measured using a IR camera (FLIR model: A655sc, accuracy: $\pm 2^\circ\text{C}$ or $\pm 2\%$ of reading), confirming
 243 the uniform distribution on the entire surface. The room temperature and pressure are $T_\infty = 287.8 \text{ K}$,
 244 $P_\infty = 102.47 \text{ kPa}$, respectively.

245 Figure 5 (a) shows the image pixel intensity distribution around the vertical hot plate. The parallel
 246 light beam passes through the width direction of the vertical plate. The schlieren image is captured
 247 using the graded-filter edge at the vertical-cutoff orientation. Therefore, the density is calculated using
 248 the one-dimensional Poisson equation because the density gradient appears at only x-direction.
 249 Thereafter, the density value is converted to a temperature using the ideal gas law. The temperature
 250 distributions calculated by the calibrated schlieren image and similarity solution are shown in Fig. 5
 251 (b). The experimental temperature distribution is good agreement with the theoretical value. However,
 252 the temperature near the wall surface is slightly different because the light beam passing close to the
 253 wall surface is diffracted. The maximum uncertainty due to the calibrated schlieren technique is 0.80%.
 254 The maximum temperature difference between the averaged experimental curve and the theoretical
 255 curve is 0.70% and appears near the wall surface. Generally, the optical components and arrangement
 256 affect the accuracy in the calibrated schlieren technique. As the results of the present validation, the
 257 present optical components and arrangement lead to good accuracy which is similar to the previous
 258 work [28].

259 **3. Results and discussions**

260 **3.1 Qualitative flow characteristics**

261 The shock waves as well as the thermal disturbance above the actuator are formed due to the rapid
 262 local gas heating. The qualitative density field shown in Fig. 6 was captured using the high-speed

263 schlieren technique with the circular dot cut-off plate. The density gradient captured using the circular
264 dot plate is sensitive to both directions on the x-y plane. As shown in Fig. 6 (a), a hemi-cylindrical
265 shock wave and a quasi-planar shock wave propagate from the edge of the exposed electrode and from
266 the plasma streamers, respectively. The shock wave formation observed in the present experiment is
267 identical to previous investigations [17, 24, 30]. Note that the shadow above the exposed electrode is
268 the polyimide film that covers the lateral side edge of the exposed electrode and the connection cable
269 (see Fig. 1), thus we can neglect the physical effect of the shadow on the shock wave formation as well
270 as the thermal disturbance. The plasma streamers propagate towards the ground electrode [3], and the
271 surrounding gas of the plasma streamers is rapidly heated because of the relatively higher temperature
272 of the plasma layer. According to temperature measurements of the plasma layer [16], the temperature
273 increases by 40 K during the discharge phase at an input voltage of 18 kV in the first pulse. The thermal
274 disturbance is not clearly observed at the elapsed time of approximately 0.14 μs in the schlieren image
275 (Fig. 6 (a)), whereas the shock waves have already formed. Although the surrounding gas is heated by
276 the plasma discharge, the heated gas would be stationary at the elapsed time of approximately 0.14 μs .
277 Since the thickness of the exposed electrode is 35 μm , the plasma layer would be thin; thus, density
278 change of the plasma layer is barely visible immediately after the first plasma discharge event. At the
279 elapsed time of 0.5 ms (Fig. 6 (b)), the thermal layer can be observed as well as a hot plume. The hot
280 plume is generated from the edge of the exposed electrode. Once a second plasma discharge event
281 elapses (Fig. 6 (c)), the second shock waves are formed; thereafter, the thermal layer and the hot plume
282 grow slightly at the elapsed time of 1.5 ms (Fig. 6 (d)).

283 The hot plume is advected towards the ground electrode due to a low-speed induced flow. After the
284 elapsed time of 4 ms (from Fig. 6 (e)), a small hot plume from the edge of the exposed electrode
285 appears and moves towards the ground electrode. A smoke experiment by Roupasov *et al.* [3] showed
286 that induced velocity is not zero, thus the hot plume shown in the present experiment is advected due
287 to the very low-speed ionic wind. The reason why the transfer of the hot plume cannot be observed in
288 the present schlieren images at the range of the elapsed time of 0 and 4 ms is that the hot plume is
289 relatively weak and propagates at a very slow velocity. Additionally, the plasma discharge would not
290 generate a strong ionic wind at an early-stage of the actuator operation. Even though 5 ms elapsed
291 from the first plasma discharge (Fig. 6 (j)), the entire hot plume ascends due to the thermal convection;
292 however, the hot plume gradually moves towards the ground electrode. This is because the low-speed
293 ionic wind starts influencing the hot plume. The colour schlieren image, which shows the time-
294 averaged density gradient of 2.5 ms, clearly captures the subsequent flow field of the advection event
295 (Fig. 7). The orientation of the colour filter wheel used in the present experiment is also shown in Fig.
296 7. The undisturbed density field is indicated by the blue colour. The parallel light beam close to the

297 edge of the exposed electrode bends towards the x-direction; namely, the hot plume moves towards
298 the ground electrode due to forced convection. Additionally, it seems that the hot plume moves towards
299 the upper right diagonal of the image. The ionic wind and/or an induced jet might cause the movement
300 of the hot plume. On the other hand, the light beam above the ground electrode bends towards the y-
301 direction; thus, natural convection caused by buoyancy force is dominant because the very weak ionic
302 wind does not influence the heated gas (thermal layer) above the ground electrode. Since the hot plume
303 leads to density change in both x- and y-direction, it is difficult to identify the hot plume in Fig. 7,
304 whereas the green colour image appearing above the ground electrode is the thermal layer growing by
305 buoyancy.

306 Although the shock wave interacts with the hot plume and thermal layer, the shock wave interaction
307 should not strongly influence the thermal flow. As shown in Fig. 6, the shock wave propagates from
308 the electrodes to surrounding air, interacting with the hot plume as well as the thermal layer. However,
309 it seems that the thermal flow pattern hardly varies due to the shock wave interaction. According to an
310 experiment [31] that the effect of shock Mach number on gas bubble motion in a different density gas
311 was investigated, in the case that an weak incident shock Mach number ($M \approx 1$) impinges on the bubble,
312 the shape of a gas bubble with similar density to a surrounding gas hardly changes, whereas a large
313 incident shock Mach number distorts the shape of the bubble. A shock wave generated from the ns-
314 DBD plasma actuator operated by few kilovolt propagates at approximately Mach 1 [20]. Therefore,
315 the hot plume and thermal layer does not strongly alter due to the shock wave interaction.

316 **3.2 Quantitative flow characteristics**

317 The calibrated schlieren technique converts the raw schlieren image to a quantitative density field.
318 Figure 8 shows the typical schlieren images at the elapsed time of 5 ms. Around the edge of the exposed
319 electrode, a strong density change in the x-direction is present (Fig. 8 (a)); namely, it denotes the hot
320 plume. The hot plume consists of the density change in the y-direction as well (Fig. 8 (b)). However,
321 the thermal layer generated above the ground electrode is hardly observed in the density change of the
322 x-direction. This is because the thermal layer, which would be not strongly affected by the ionic wind
323 and the induced jet, ascends in the y-direction due to natural convection. Figure 9 shows the refraction
324 angle distribution that is converted from the schlieren images of Fig. 8 through calibration. It is
325 assumed that the induced flow by the ns-DBD plasma actuator is a two-dimensional phenomenon. An
326 actual thermal flow generated by the plasma actuator is not a perfectly two-dimensional phenomenon;
327 however, the thermal flow in the vicinity of the plasma actuator would be two dimensional after time
328 has elapsed. Note that the $x = 0$ mm indicates the edge of the exposed electrode. Moreover, the
329 refraction angle distribution in the region where $y \leq 1$ mm is unreliable as the light beam passing close

330 to the wall surface is diffracted; therefore, the uncertainty here would be large for the quantitative
331 process. The refraction angle distribution, which is shown above $y = 1$ mm, is qualitatively the same
332 as that of the image pixel intensity distribution of the schlieren images, but the refraction angle is
333 quantifiable. The spatial density distribution, which is normalised by atmospheric density ρ_∞ , is shown
334 in Fig. 10. The hot plume appears between $x = 1$ and 2 mm above the ground electrode. Additionally,
335 the thermal layer is extended to approximately $x = 6$ mm at the elapsed time of 5 ms.

336 The hot plume is enhanced due to several plasma discharges. Temporal variation of the spatial
337 density distribution is shown in Fig. 11. The hot plume grows slightly at the elapsed time of 10 ms
338 (Fig. 11 (a)); thereafter, the density caused by the hot plume decreases locally at the coordinate (x, y)
339 $= (2, 1)$ (from Fig. 11 (b) to 11 (f)). The movement of the whole hot plume towards the upper right
340 diagonal is apparent from the spatial density distribution. The same behaviour is observed in the
341 qualitative images captured using the high-speed schlieren technique (Fig. 6). Figure 12 shows the
342 density distribution along $y = 1$ mm. At the elapsed time of 1.0 ms that the second plasma discharge
343 occurs, an almost uniform density distribution appears, although a weak density change can be
344 observed at $x = 1$ mm. It is worth noting that the first plasma discharge occurs at the elapsed time of
345 approximately 0 ms. At the elapsed time of 2.0 ms, the weak density change grows; namely, it denotes
346 the hot plume. Since thermal convection by the plasma discharge does not immediately enhance the
347 hot plume, both first and second plasma discharges cause the strong density change at the elapsed time
348 of 2.0 ms. Although several plasma discharges cause the local density change, it seems that the
349 enhancement of the density gradually decays from the elapsed time of 30 ms. This conclusion is
350 reached because the minimum density of the hot plume changes 3.3% between the elapsed time of 0
351 and 10 ms, whereas it changes only 0.4% between the elapsed time of 30 and 50 ms.

352 The density of the hot plume is equilibrated with the surrounding gas density within several tens of
353 milliseconds. The primary plasma discharges increase the gas temperature of the surrounding plasma
354 layer; consequently, the density rapidly decreases within 3 ms (see Fig. 13). It is believed that the
355 plasma-induced flow (the ionic wind and the induced jet) do not strongly affect the surrounding gas at
356 this stage. At $x = 0$ mm, corresponding to the edge of the exposed electrode (Fig. 13), the density
357 increases slightly after the rapid decrease. The ionic wind and/or the induced jet would begin to have
358 an impact here, which results in this event. Thereafter, the density becomes almost uniform after the
359 elapsed time of 20 ms. The density history at $x = 1$ mm is similar to that of $x = 0$ mm; namely, the
360 density change from 5 to 20 ms is caused by the ionic wind and/or the induced jet. However, the density
361 at $x = 1$ mm is lower than the density at $x = 0$ mm. This is a result of the hot plume growth towards the
362 ground electrode. The movement of the hot plume leads to a further density decrease at the $x = 2$ mm
363 location, which results in a density ratio of approximately 0.95 at the elapsed time of approximately

364 40 ms. Then, the density becomes uniform. At the $x = 3$ and 4 mm locations, the density did not
 365 decrease significantly compared with the $x = 2$ mm case; nevertheless, the plasma-induced flow is still
 366 apparent. This is because the core of the hot plume does not extend to more than $x = 3$ mm (Fig. 11
 367 (f)). As shown in Fig. 13, the density is almost uniform after the elapsed time of 40 ms although the
 368 density at $x = 3$ and 4 mm keeps decreasing slightly. The reason why the density gradually decreases
 369 is due to natural convection of the thermal layer formed above the ground electrode.

370 The heated gas which moves away from the wall surface is not influenced by the plasma-induced
 371 flow (the ionic wind and the induced jet). Figure 14 shows the density profile along the y -coordinate.
 372 In the spatial density distribution above $y = 1$ mm, the first plasma discharge barely contributes to the
 373 hot plume enhancement. Consequently, both density profiles of the $x = 2$ and 3 mm positions at the
 374 elapsed time of 1 ms are similar to the temperature profile due to natural convection on a horizontal
 375 heated plate [32]. At the elapsed time of 5 ms, it can be observed that the thermal layer is slightly
 376 distorted around $y = 2$ mm along $x = 2$ mm (Fig. 14 (a)). This is because the hot plume starts disturbing
 377 the thermal layer formed by the plasma layer. Note here that close to the wall surface (below $y = 1$
 378 mm), the hot plume would start disturbing the thermal layer relatively early. In the density profile
 379 along $x = 3$ mm (Fig. 14 (b)), the heated gas, which is generated by the primary discharges, begins to
 380 ascend after the elapsed time of 5 ms. The round-shaped profile appearing at the $y = 5$ mm location at
 381 the elapsed time of 20 ms moves to $y = 8$ mm, 20 ms later (Fig. 14 (b)). Even when the time elapses,
 382 the density intensity of the round-shaped profile visible at $y = 5$ mm is almost the same as that at $y = 8$
 383 mm and that of $y = 10$ mm at the elapsed time of 60 ms. The same behaviour occurs in the density
 384 profile along $x = 2$ mm (Fig. 14 (a)). However, this rounded shape will disappear due to thermal
 385 equilibrium in a steady state. Additionally, the density of the heated gas is equilibrated with the
 386 surrounding gas density when the heated gas moves further away from the wall surface. As shown in
 387 Fig. 11 (a) to (d), the heated gas above $y = 5$ mm ascends only in the y -direction even though the hot
 388 plume moves towards both x - and y -directions. The reason why the density intensity of the heated gas
 389 caused by the primary plasma discharges does not change above $y = 5$ mm is that the plasma-induced
 390 flow hardly influences the heated gas above $y = 5$ mm.

391 On the other hand, the density below the $y = 5$ mm location is strongly influenced by the plasma-
 392 induced flow. At the elapsed time of 5 ms (see Fig. 14), the density ratio, which is $\rho/\rho_\infty = 0.981$, at the
 393 coordinate $(x, y) = (3, 1)$ is similar to the density ratio of $\rho/\rho_\infty = 0.980$ at $(x, y) = (2, 1)$; thereafter, the
 394 density decreases slightly at the elapsed time of 20 ms, which results in a density change of 0.26%
 395 (Fig. 14 (b)). On the other hand, in the case of the density at $(x, y) = (2, 1)$, the local density decreases
 396 significantly, by 2.2%, at the elapsed time of 20 ms (Fig. 14 (a)). This is because the plasma-induced
 397 flow, which is the ionic wind and the induced jet, at first starts influencing the density field close to

398 the edge of the exposed electrode. At the elapsed time of 40 ms, the density at $(x, y) = (3, 1)$ strongly
399 decreases due to the hot plume being moved by the plasma-induced flow (Fig. 14 (b)). Moreover, the
400 peak of the density decrease along $x = 3$ mm is located around $y = 2$ mm because the hot plume moves
401 upwards along the y -direction.

402 **4. Conclusion**

403 Qualitative and quantitative schlieren techniques were employed to investigate the spatial density
404 distribution above a nanosecond pulsed dielectric barrier discharge (ns-DBD) plasma actuator in
405 quiescent air. Consequently, qualitative schlieren showed that rapid heating at the edge of the exposed
406 electrode generates a hemi-cylindrical shock wave and a hot plume. The hot plume is advected towards
407 the ground electrode due to a low-speed induced flow which is caused by an ionic wind and/or an
408 induced jet. On the other hand, the thermal layer formed due to thermal convection of the plasma
409 streams above the ground electrode was not influenced by the low-speed induced flow. The
410 quantitative schlieren revealed the detailed density distribution. The density of the hot plume was
411 enhanced due to several plasma discharges; however, the density is equilibrated with the surrounding
412 gas density within several tens of milliseconds. Moreover, the heated gas which moves away from the
413 wall surface was not influenced by the plasma-induced flow (the ionic wind and the induced jet),
414 whereas the plasma-induced flow strongly influenced the density below $y = 5$ mm. This study showed
415 the initial temporal variation of the spatial density distribution above the ns-DBD plasma actuator in
416 quiescent air. Understanding how the thermal characteristics in quiescent air conditions interacts with
417 a boundary layer is important for a better understanding for the mechanism of boundary layer transition.

418 Nanosecond pulsed DBD plasma actuators provide thermal perturbation caused by local high
419 energy transfer, and the thermal perturbation mainly leads to turbulent boundary layer transition. The
420 fundamental thermal flow behaviour shown in this study is that the thermal spot (hot plume) is locally
421 generated and moves slightly. The possible scenario of the turbulent transition is that the local hot
422 plume leads to strong and complicated thermal perturbation. The further studies focusing on the
423 investigation of the energy transfer from the hot plume to the surrounding gas are important for the
424 optimization of the ns-plasma actuators.

425 **Acknowledgments**

426 This research work was supported by the European Commission, H2020-MSCA-IF (Project reference:
427 654318).

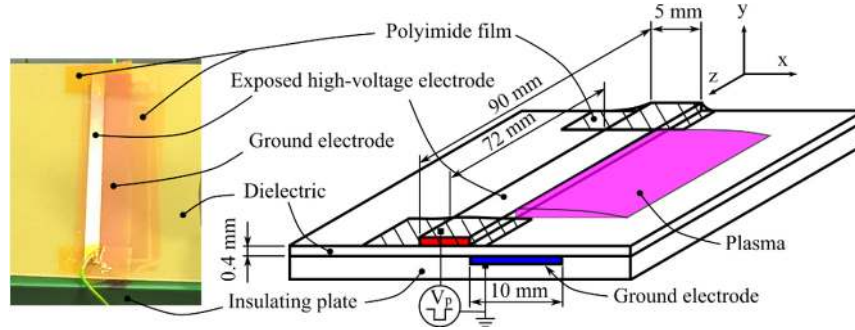
428 References

- 429 [1] Y. Xiao¹, S.J. Dai, L.M. He, T. Jin, Q. Zhang, P.H. Hou, “Investigation of film cooling from
430 cylindrical hole with plasma actuator on flat plate,” *Heat Mass Transfer* 52, pp.1571-1583
431 (2016).
- 432 [2] P. Audier, M. Fenot, N. Benard, E. Moreau, “Film cooling effectiveness enhancement using
433 surface dielectric barrier discharge plasma actuator,” *Int. J. Heat Fluid Flow* 62, pp.247-257
434 (2016).
- 435 [3] D.V. Roupasov, A.A. Nikipelov, M.M. Nudnova, A.Yu. Starikovskii, “Flow Separation
436 Control by Plasma Actuator with Nanosecond Pulsed-Periodic Discharge,” *AIAA J.* 47 (1),
437 pp.169-185 (2009).
- 438 [4] J.R. Roth, “Aerodynamic flow acceleration using paraelectric and peristaltic
439 electrohydrodynamic effects of a One Atmosphere Uniform Glow Discharge Plasma,” *Phys.*
440 *Plasmas* 10, pp.2117-2126 (2003).
- 441 [5] M. Riherd, S. Roy, “Serpentine geometry plasma actuators for flow control,” *J. Appl. Phys.*
442 114, 083303 (2013).
- 443 [6] S. Roy, P. Zhao, A. DasGupta, J. Soni, “Dielectric barrier discharge actuator for vehicle drag
444 reduction at highway speeds,” *AIP Adv.* 6, 025322 (2016).
- 445 [7] R. Spivey, R. Hewitt, H. Othman, T. Corke, “Flow Separation Control on Trailing Edge
446 Radii using Single Dielectric Barrier Discharge Plasma Actuators: An Application to Vehicle
447 Drag Control,” *The Aerodynamics of Heavy Vehicles II: Trucks, Buses, and Trains* pp 135-
448 149 (2009).
- 449 [8] N. Benard, J. Jolibois, E. Moreau, “Lift and drag performances of an axisymmetric airfoil
450 controlled by plasma actuator,” *J. Electrostat* 67, pp.133–139 (2009).
- 451 [9] K.S. Choi, T. Jukes, R. Whalley, “Turbulent boundary-layer control with plasma actuators,”
452 *Phil. Trans. R. Soc. A* 369, pp.1443-1458 (2011).
- 453 [10] R. Erfani, H. Zare-Behtash, C. Hale, K. Kontis, “Development of DBD plasma actuators:
454 The double encapsulated electrode,” *Acta Astronaut.* 109 pp.132-143 (2015).
- 455 [11] M. Forte, J. Jolibois, J. Pons, E. Moreau, G. Touchard, M. Cazalens, “Optimization of a
456 dielectric barrier discharge actuator by stationary and non-stationary measurements of the
457 induced flow velocity: application to airflow control,” *Exp Fluids* 43, pp.917-928 (2007).
- 458 [12] C.A. Borghi, A. Cristofolini, G. Neretti, P. Seri, A. Rossetti, A. Talamelli, “Duty cycle and
459 directional jet effects of a plasma actuator on the flow control around a NACA0015 airfoil,”
460 *Meccanica* 52, pp.3661–3674 (2017).

- 461 [13] N. Benard, E. Moreau, “Capabilities of the dielectric barrier discharge plasma actuator for
462 multi-frequency excitations,” *J. Phys. D: Appl. Phys.* 43, 145201 (2010).
- 463 [14] F.O. Thomas, T.C. Corke, M. Iqbal, A. Kozlov, D. Schatzman, “Optimization of Dielectric
464 Barrier Discharge Plasma Actuators for Active Aerodynamic Flow Control,” *AIAA J.* 47 (9)
465 pp.2169-2178 (2009).
- 466 [15] K. Kinefuchi, A.Y. Starikovskiy, R.B. Miles, “Numerical investigation of nanosecond pulsed
467 plasma actuators for control of shock-wave/boundary-layer separation,” *Phys. Fluids* 30,
468 106105 (2018).
- 469 [16] A.Y. Starikovskii, A.A. Nikipelov, M.M. Nudnova¹, D.V. Roupasov, “SDBD plasma
470 actuator with nanosecond pulse-periodic discharge,” *Plasma Sources Sci. Technol.* 18,
471 034015 (2009).
- 472 [17] R. Dawson, J. Little, “Characterization of nanosecond pulse driven dielectric barrier
473 discharge plasma actuators for aerodynamic flow control,” *J. Appl. Phys* 113, 103302 (2013).
- 474 [18] G. Correale, T. Michelis, D. Ragni, M. Kotsonis, F. Scarano, “Nanosecond-pulsed plasma
475 actuation in quiescent air and laminar boundary layer,” *J. Phys. D: Appl. Phys.* 47, 105201
476 (2014).
- 477 [19] J.G. Zheng, Z.J. Zhao, J. Li, Y.D. Cui, B.C. Khoo, “Numerical simulation of nanosecond
478 pulsed dielectric barrier discharge actuator in a quiescent flow,” *Phys. Fluids* 26, 036102
479 (2014).
- 480 [20] Z. Zhao, Jiun-Ming Li, J. Zheng, Y.D. Cui, B.C. Khoo, “Study of shock and induced flow
481 dynamics by nanosecond dielectric-barrier-discharge plasma actuators,” *AIAA J.* 53 (5),
482 pp.1336-1348 (2015).
- 483 [21] A. Komuro, K. Takashima, K. Konno, N. Tanaka, T. Nonomura, T. Kaneko, A. Ando, K.
484 Asai, “Schlieren visualization of flow-field modification over an airfoil by near-surface gas-
485 density perturbations generated by a nanosecond-pulse-driven plasma actuator,” *J. Phys. D:
486 Appl. Phys.* 50 215202 (2017).
- 487 [22] D. Hai, S. Zhiwei, C. Keming, L. Ganniu, L. Jichun, L. Zheng, H. Liang, “The study of flow
488 separation control by a nanosecond pulse discharge actuator,” *Exp. Therm. Fluid Sci.* 74
489 pp.110–121 (2016).
- 490 [23] D. Ullmer, P. Peschke, A. Terzis, P. Ott, B. Weigand, “Impact of ns-DBD plasma actuation
491 on the boundary layer transition using convective heat transfer measurements,” *J. Phys. D:
492 Appl. Phys.* 48 365203 (2015).
- 493 [24] J. Little, K. Takashima, M. Nishihara, I. Adamovich, M. Samimy, “Separation Control with
494 Nanosecond-Pulse-Driven Dielectric Barrier Discharge Plasma Actuators,” *AIAA J.* 50 (2),

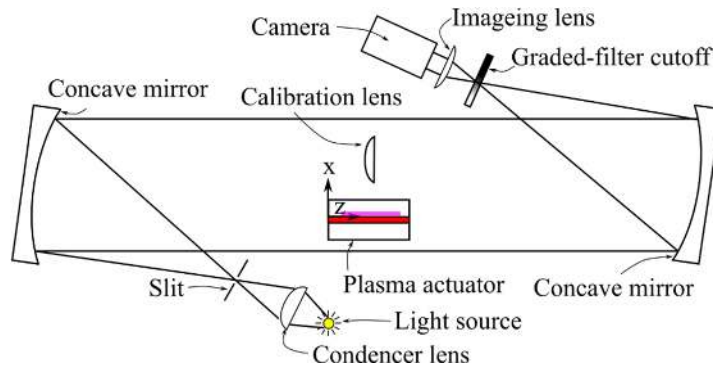
- 495 pp.350-365 (2012).
- 496 [25] A. Russell, H. Zare-Behtash, K. Kontis, "Characterisation of ns-DBD plasma actuators for
497 supersonic flow control," Proceedings of 30th of the International Council of the Aeronautical
498 Sciences 2016.
- 499 [26] R.A. Dawson, J. Little, "Effects of pulse polarity on nanosecond pulse driven dielectric
500 barrier discharge plasma actuators," *J. Appl. Phys* 115, 043306 (2014).
- 501 [27] G.S. Settles 'Schlieren and shadowgraph techniques: Visualizing phenomena in transparent
502 media,' Springer (2001).
- 503 [28] M.J. Hargather, G.S. Settles, "A comparison of three quantitative schlieren techniques,"
504 Optics and Lasers in Engineering 50, pp.8-17 (2012).
- 505 [29] S. Ostrach, "An analysis of laminar free-convection flow and heat transfer about a flat plate
506 parallel to the direction of the generating body force," NACA Technical Report 2635 (1952).
- 507 [30] K. Takashima, Y. Zuzeek, W.R. Lempert, I.V. Adamovich, "Characterization of a surface
508 dielectric barrier discharge plasma sustained by repetitive nanosecond pulses," *Plasma
509 Sources Sci. Technol.* 20, 055009 (2011).
- 510 [31] G. Layes, G. Jourdan, L. Houas, "Experimental study on a plane shock wave accelerating a
511 gas bubble," *Phys. Fluids* 21, 074102 (2009).
- 512 [32] L. Pera, B. Gebhart, "Natural convection boundary layer over horizontal and slightly
513 inclined surfaces," *Int. J. Heat Mass Transfer* 16, pp.1131-1146 (1973).

514 **Figures**



515

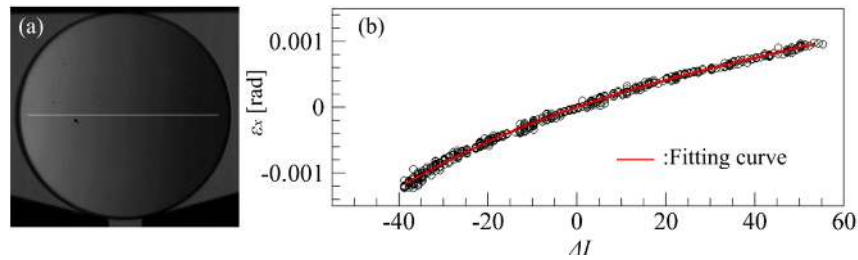
516 Fig 1. The configuration of the ns-DBD plasma actuator (Left figure: the actual plasma actuator used
517 in the study).



518

519

Fig 2. Optical arrangement of the calibrated schlieren photography.

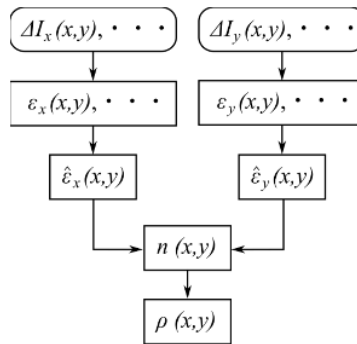


520

521 (a): Image pixel intensity change due to the calibration lens, (b): Calibration curve obtained from the
522 location indicating a white line shown on the calibration lens.

523

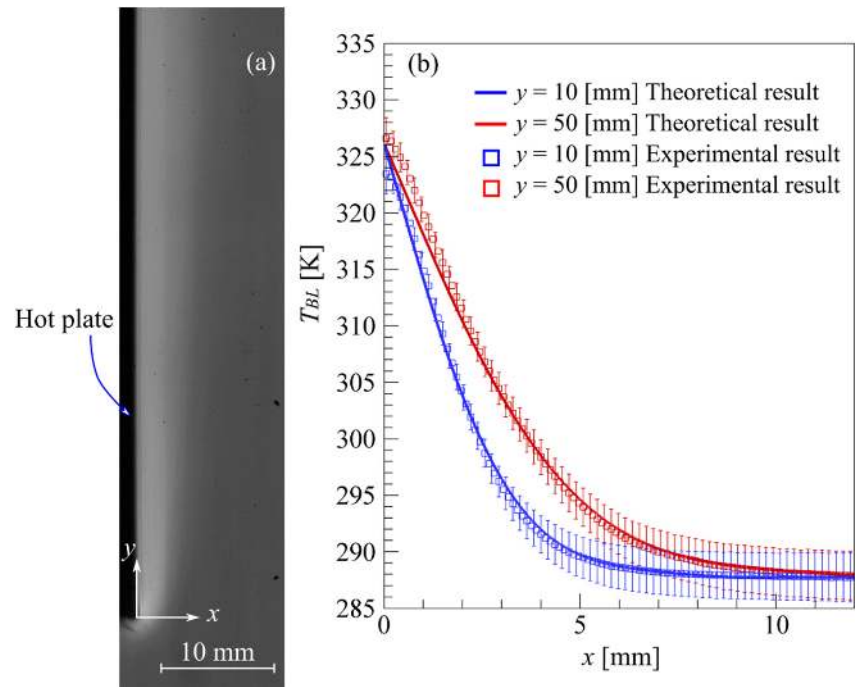
Fig 3. Calibration using the vertical graded-filter cutoff.



524

525

Fig 4. The flow chart of the procedure for the quantitative density measurement.



526

527

528

Fig 5. The temperature distribution due to the natural thermal convection around the vertical hot plate. Theoretical result denotes temperature calculated by equation 11.

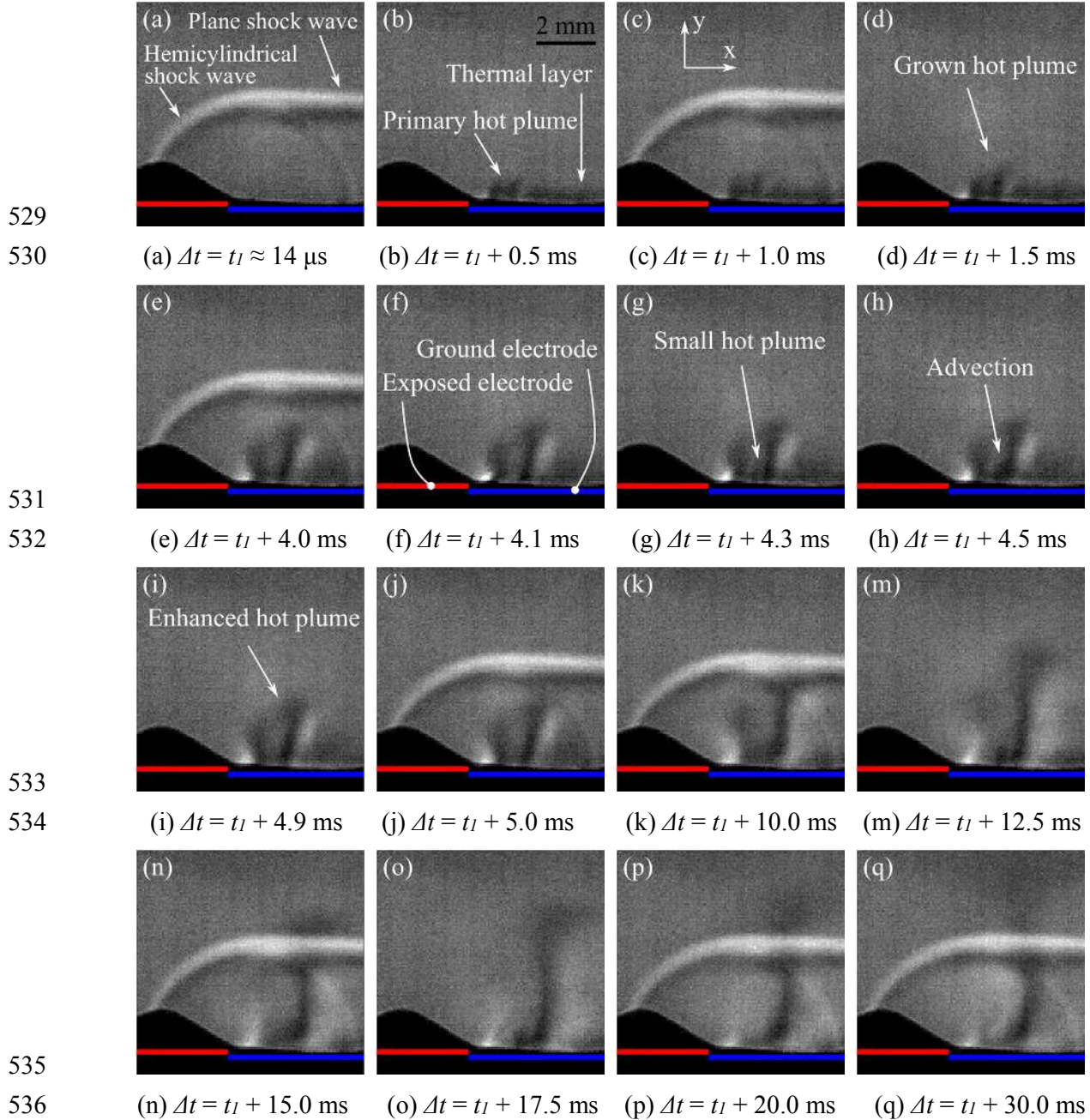


Fig 6. The formation of the hot plume, thermal layer, and the shock waves.

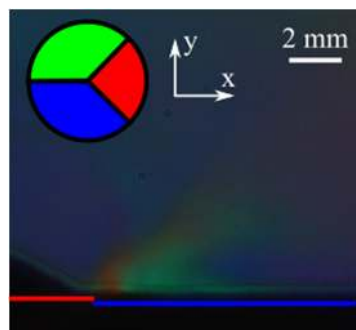


Fig 7. Colour schlieren image.



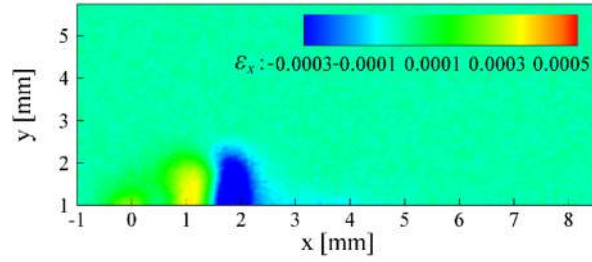
540

541

542

(a) pixel intensity change in the x-direction (b) pixel intensity change in the y-direction

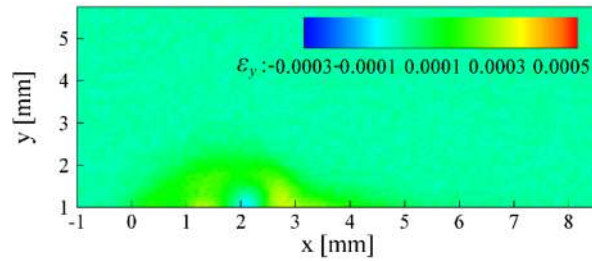
Fig 8. Typical schlieren images at $\Delta t = 5$ ms.



543

544

(a) refraction angle in the x-direction



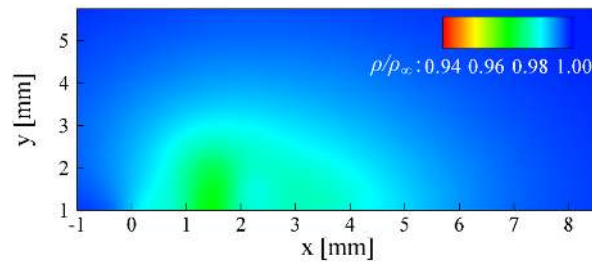
545

546

(b) refraction angle in the y-direction

547

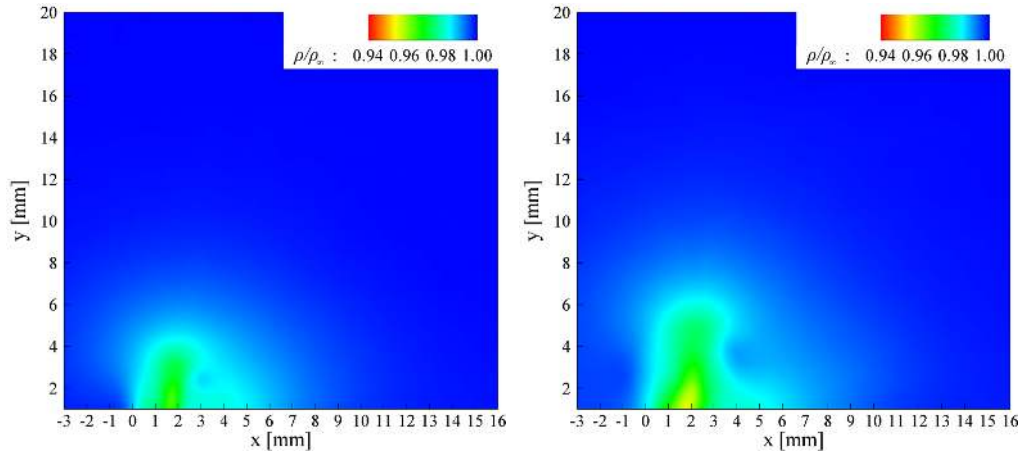
Fig 9. Ensemble average of refraction angle distribution at $\Delta t = 5$ ms.



548

549

Fig 10. Spatial density distribution at $\Delta t = 5$ ms.

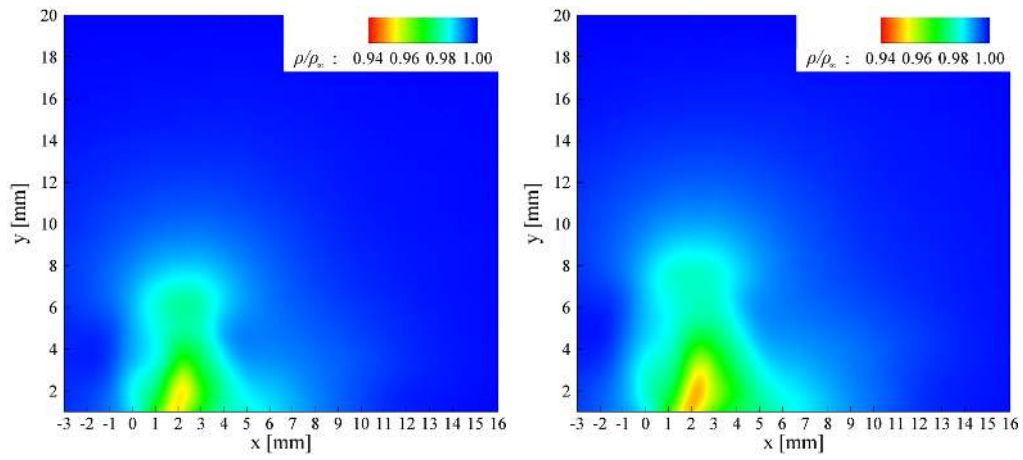


550

551

(a) $\Delta t = 10$ ms

(b) $\Delta t = 20$ ms

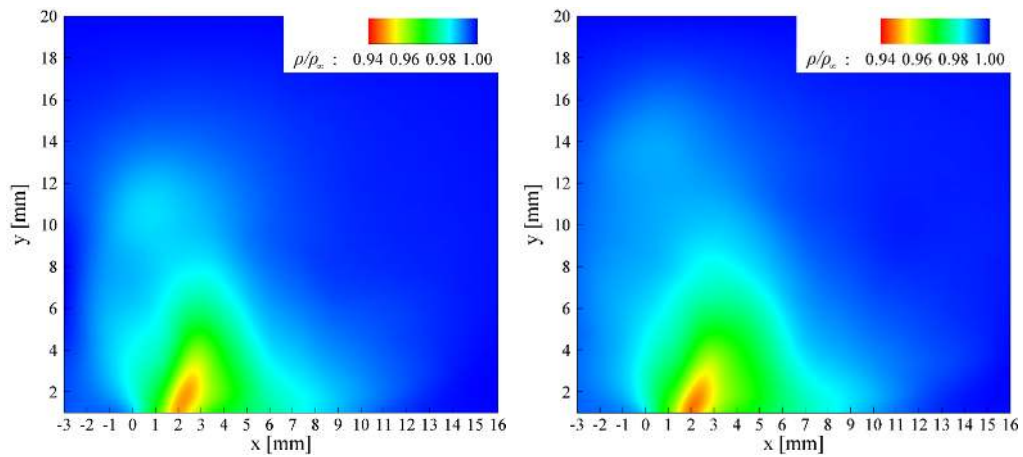


552

553

(c) $\Delta t = 30$ ms

(d) $\Delta t = 40$ ms



554

555

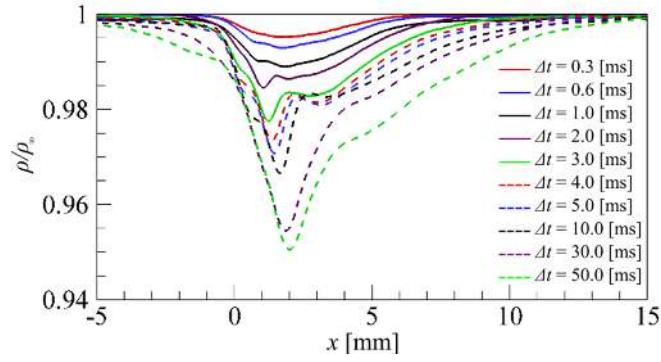
(e) $\Delta t = 70$ ms

(f) $\Delta t = 100$ ms

556 Fig 11. Temporal variation of spatial density distribution. 101 times shock wave pulses occur during

557

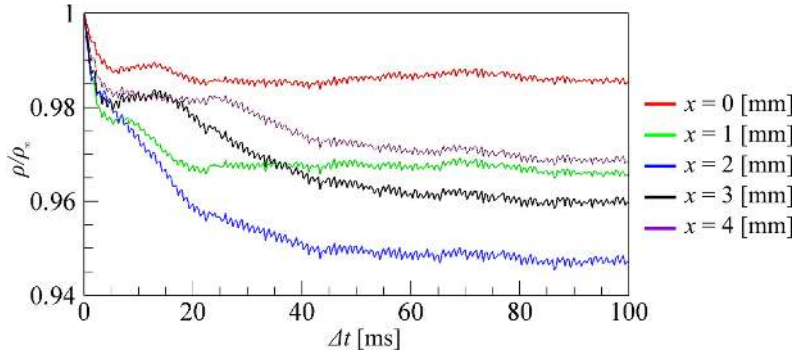
$\Delta t = 100$ ms.



558

559

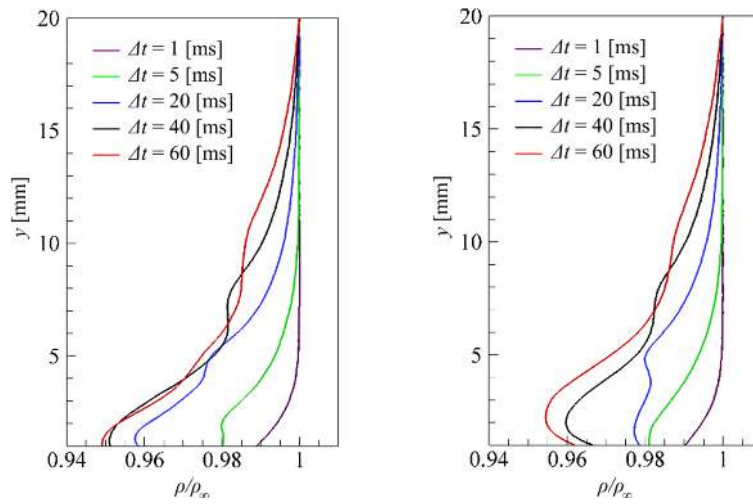
Fig 12. Density distribution at $y = 1$ mm.



560

561

Fig 13. Temporal variation of density decrease at $y = 1$ mm.



562

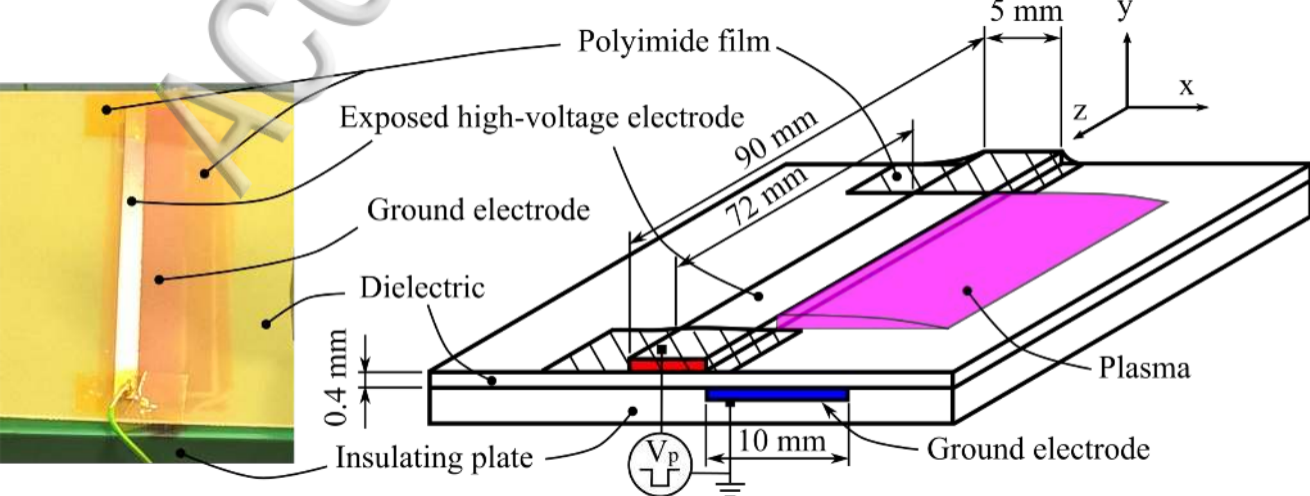
563

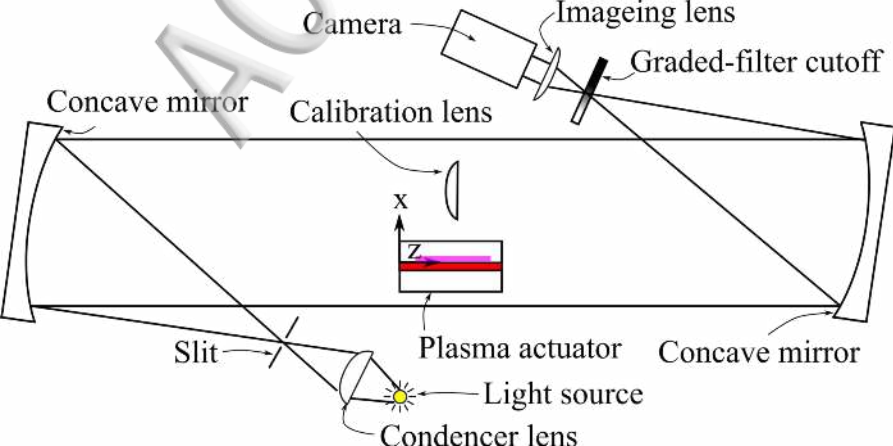
564

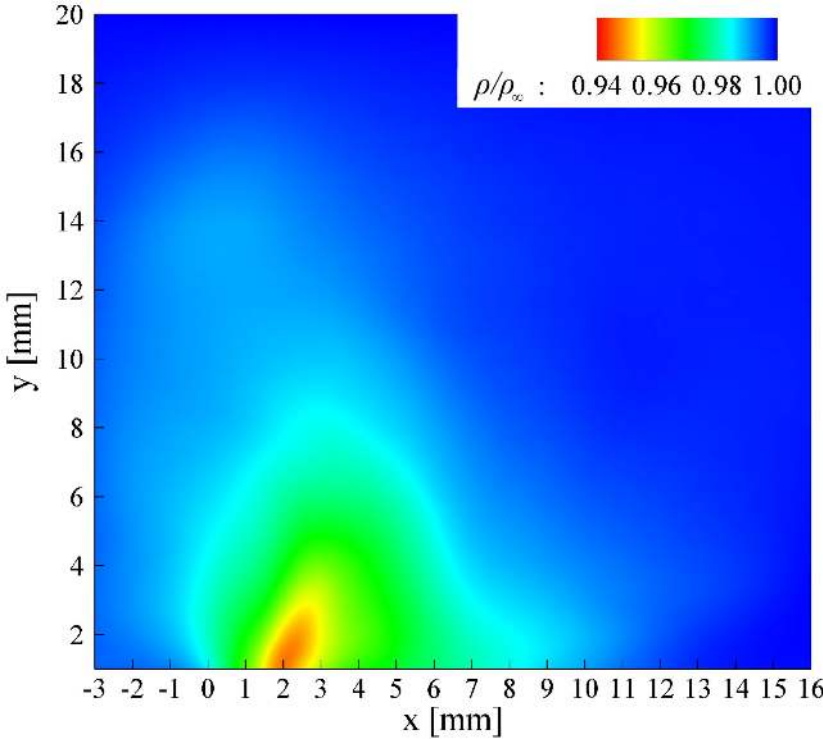
(a) $x = 2$ mm

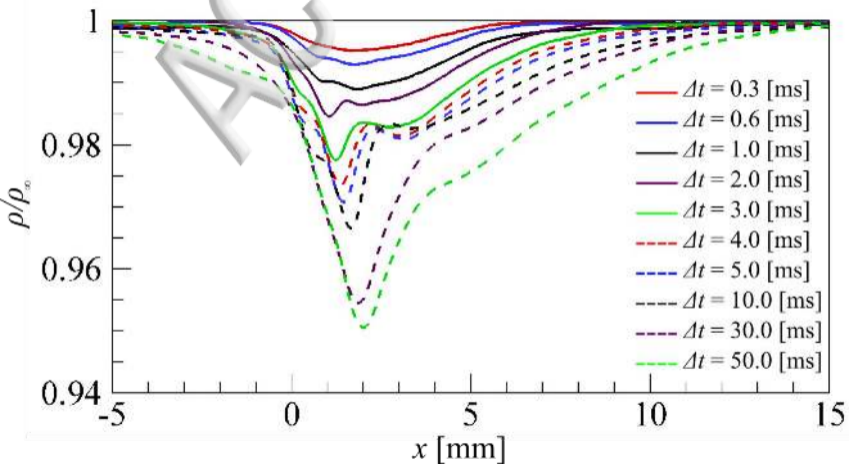
(b) $x = 3$ mm

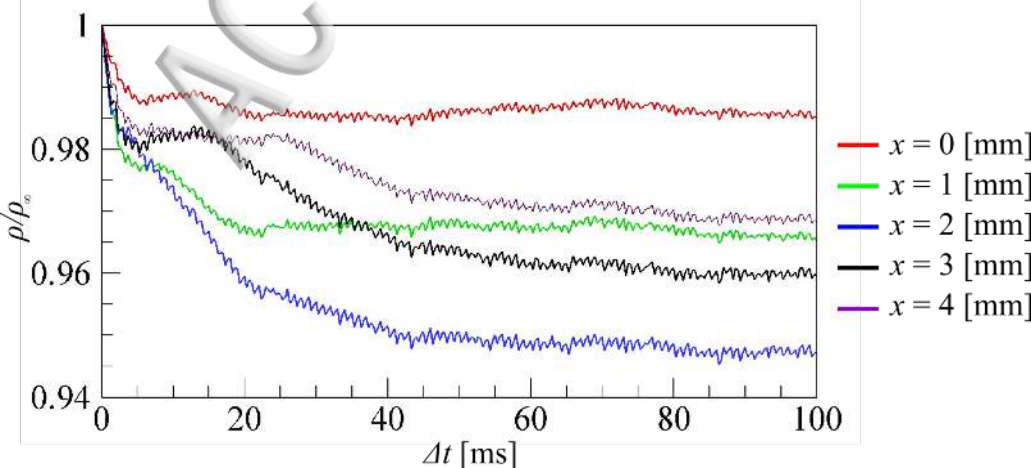
Fig 14. Thermal layer distribution.

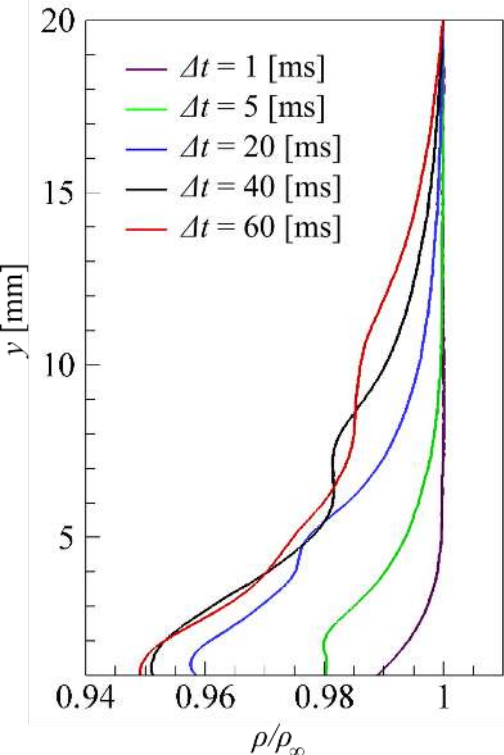


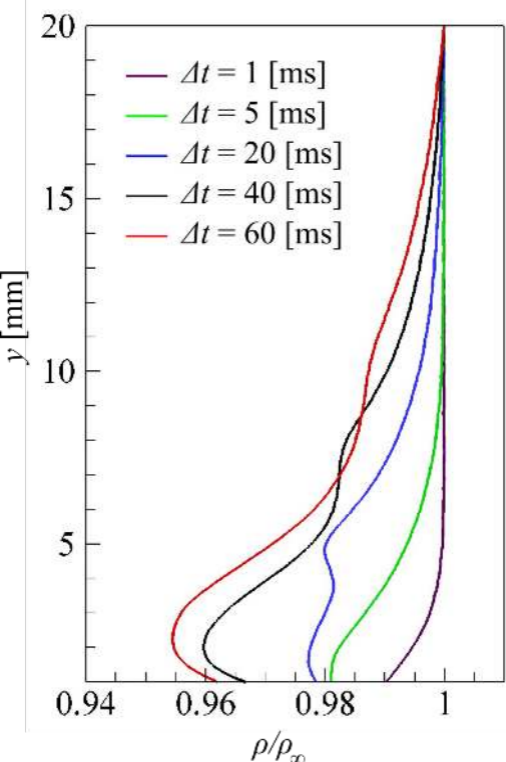


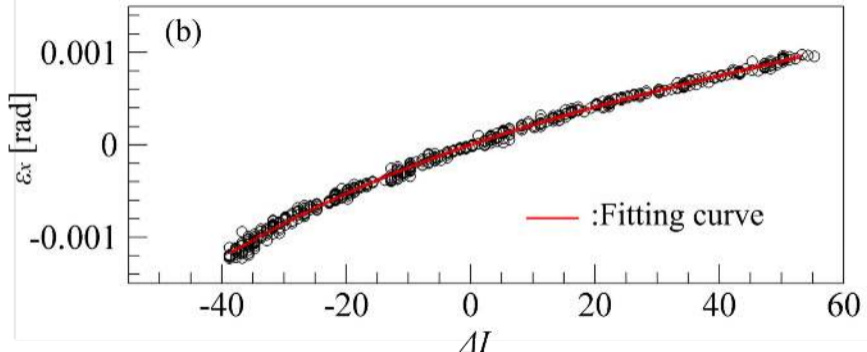
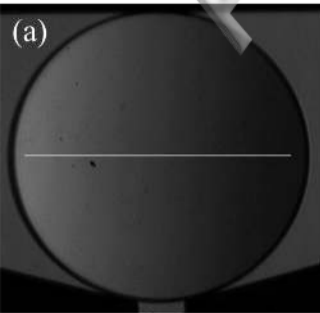


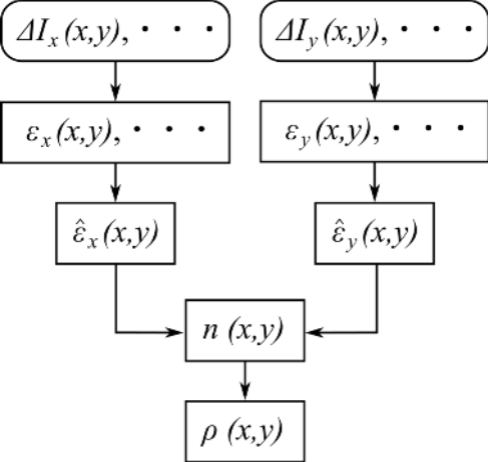


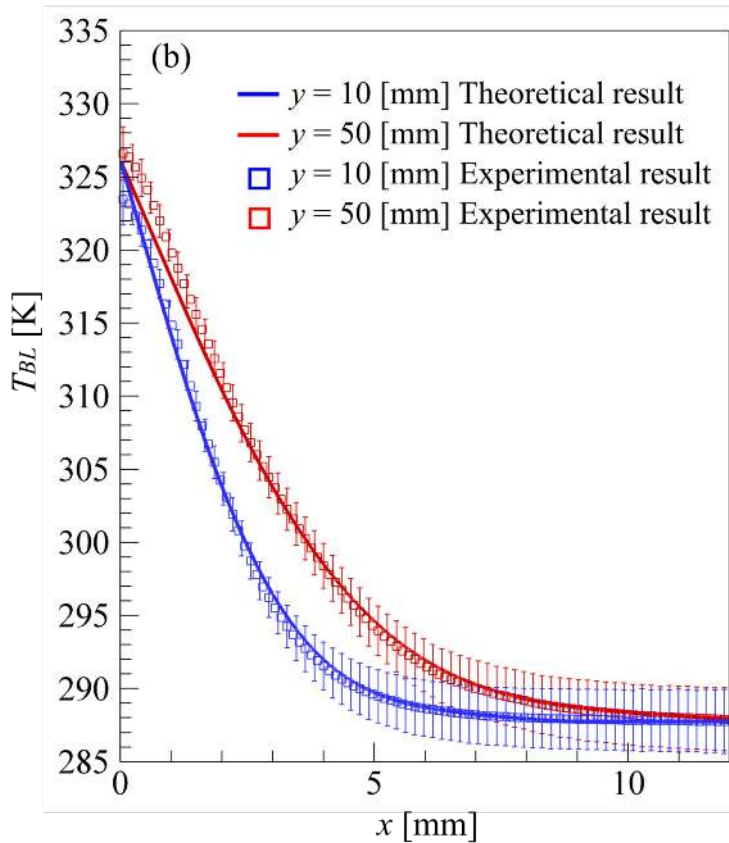
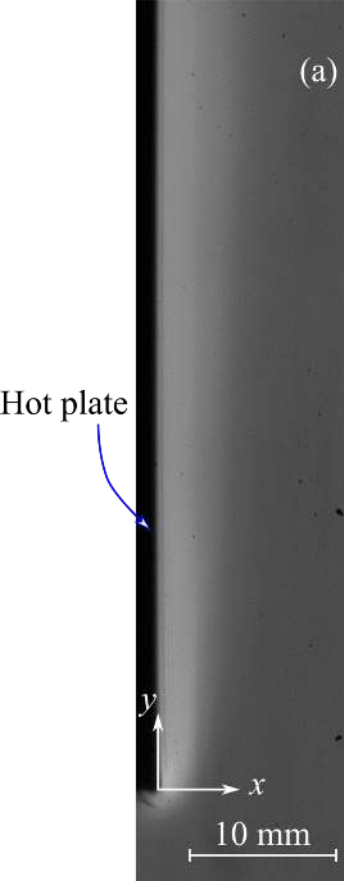














2 mm



Exposed electrode



Ground electrode

Exposed electrode



Ground electrode

y [mm]

5

4

3

2

1

-1

0

1

2

3

4

5

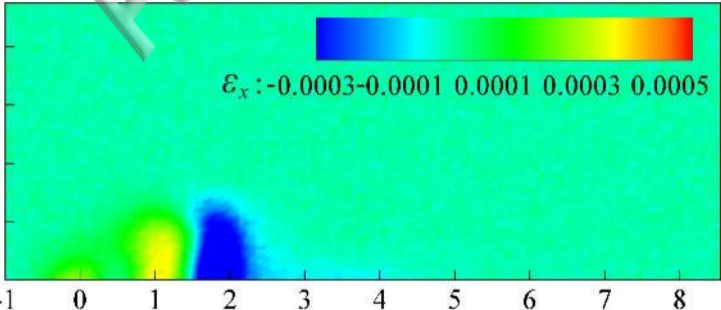
6

7

8

x [mm]

ε_x : -0.0003 -0.0001 0.0001 0.0003 0.0005



y [mm]

5

4

3

2

1

-1

0

1

2

3

4

5

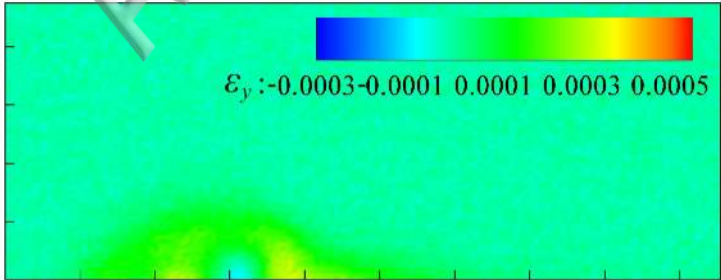
6

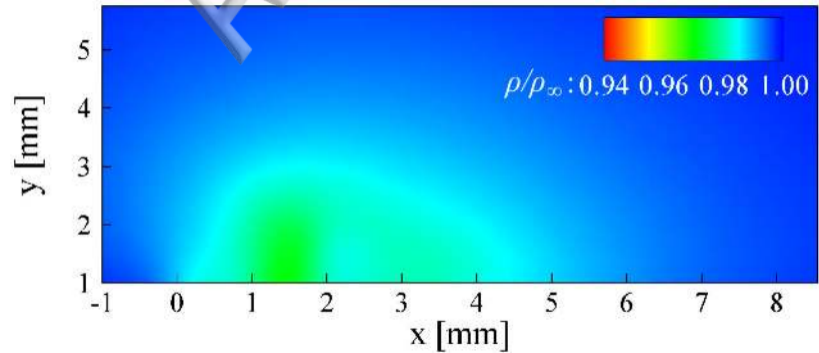
7

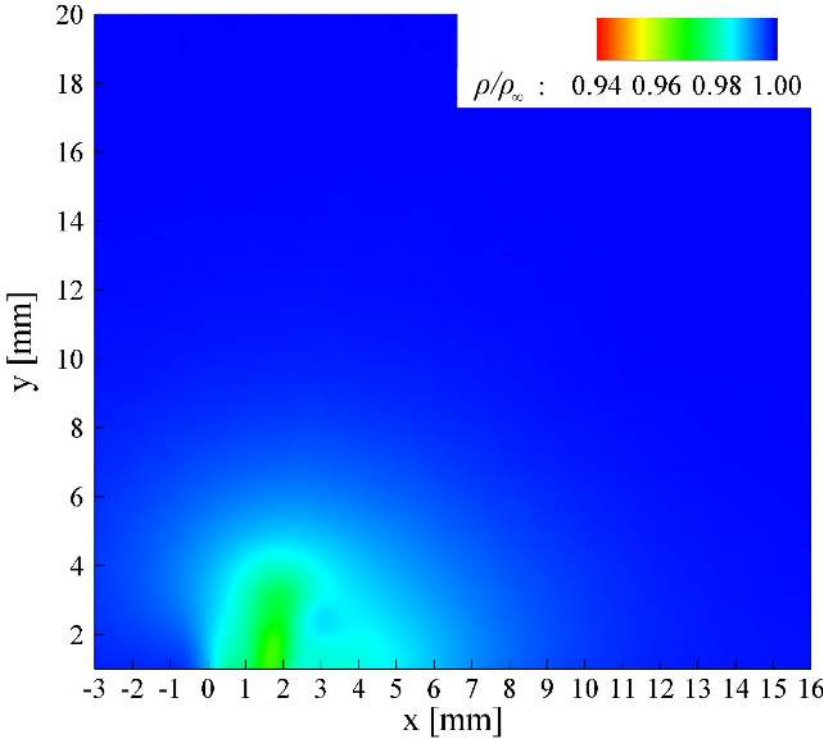
8

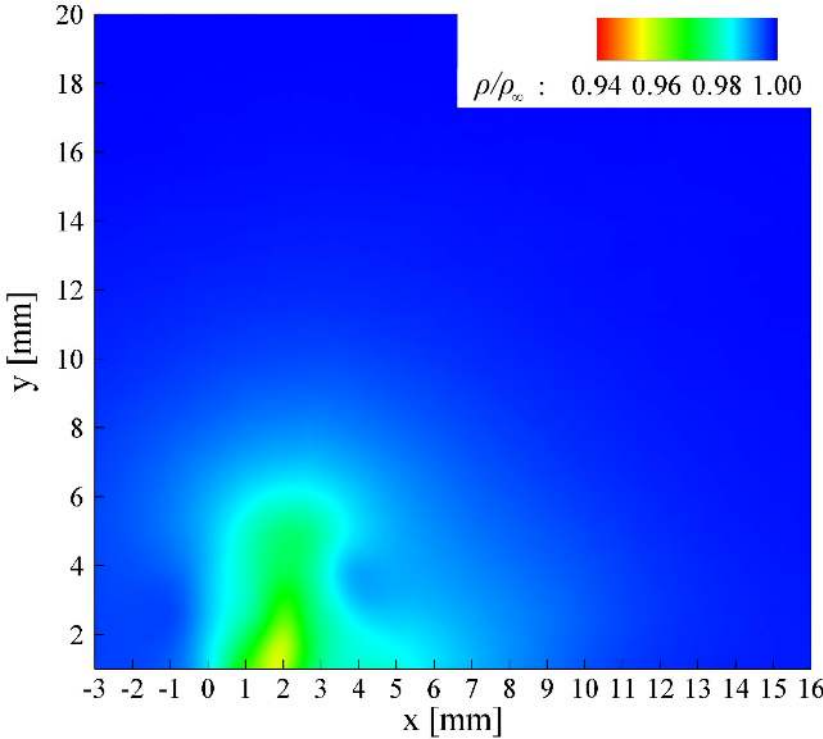
x [mm]

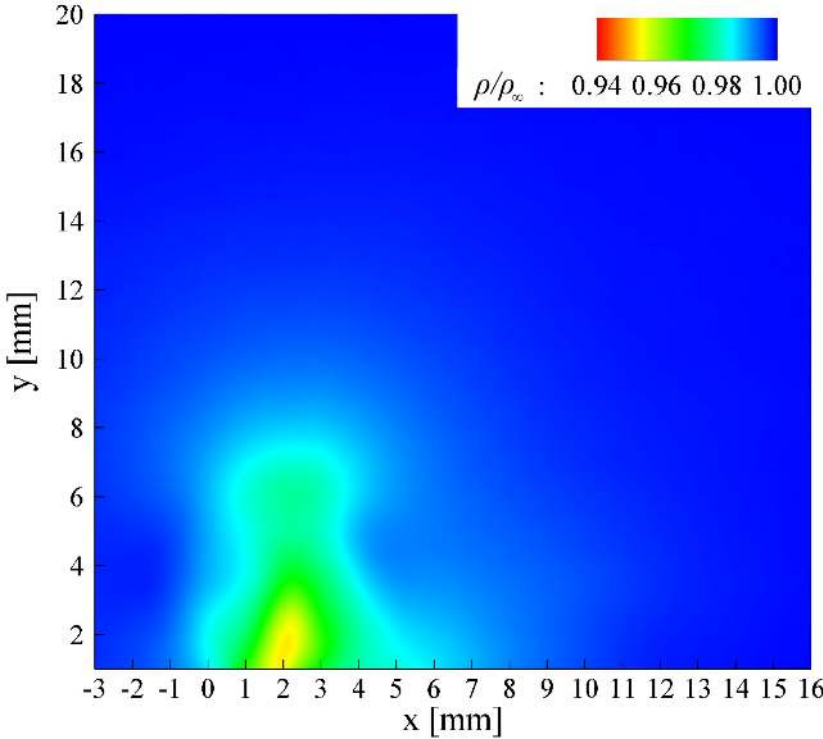
ε_y : -0.0003 -0.0001 0.0001 0.0003 0.0005

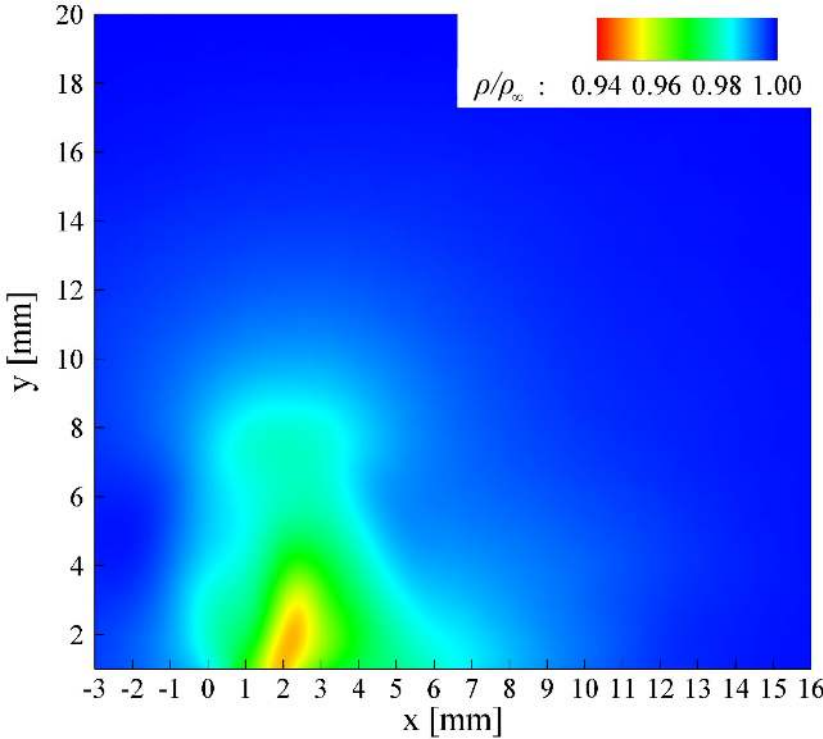


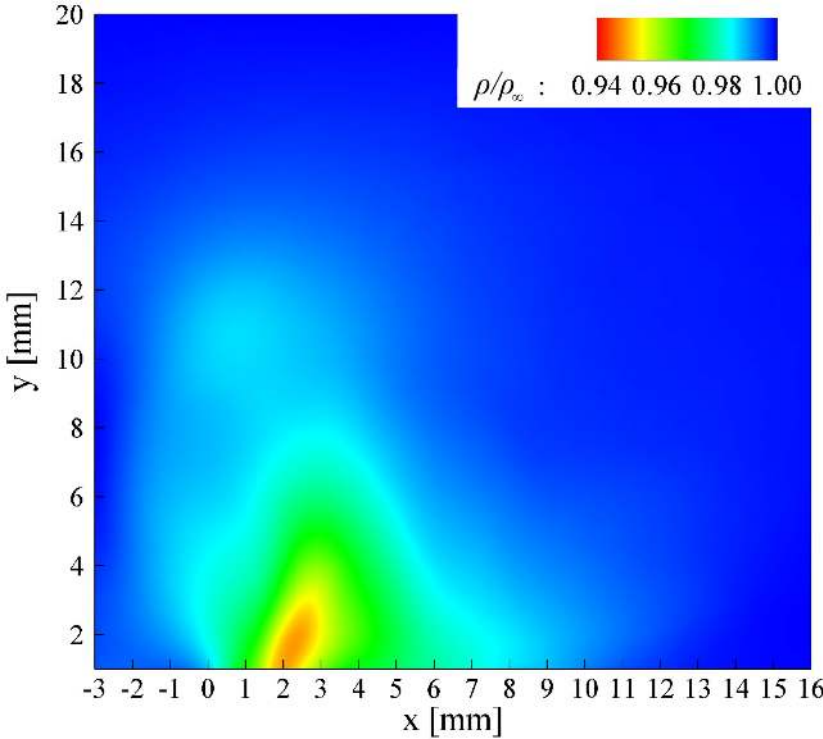












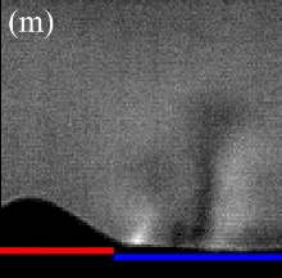
(j)



(k)



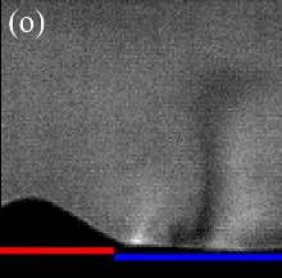
(m)



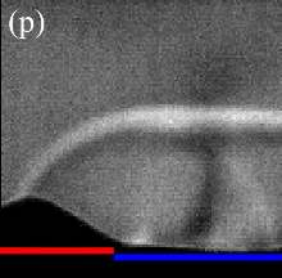
(n)



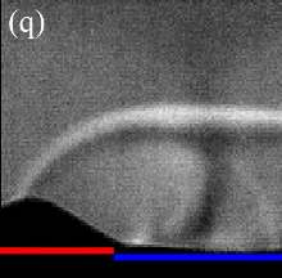
(0)



(p)

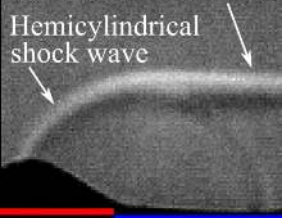


(q)



(a) Plane shock wave

Hemicylindrical
shock wave

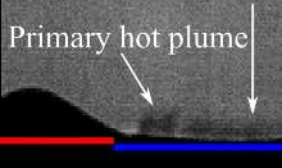


(b)

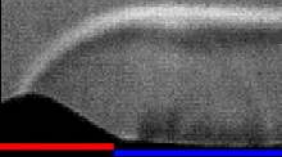
2 mm

Thermal layer

Primary hot plume

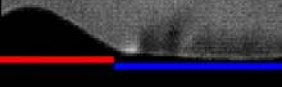


(c)

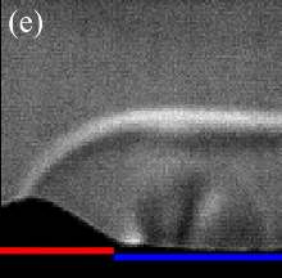


(d)

Grown hot plume



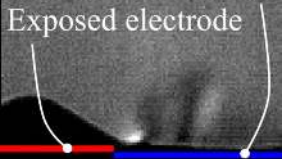
(e)



(f)

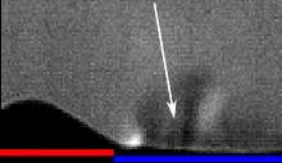
Ground electrode

Exposed electrode



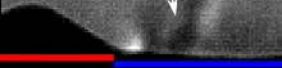
(g)

Small hot plume



(h)

Advection



(i)

Enhanced hot plume

